https://doi.org/10.1016/j.compgeo.2021.104141

Metaheuristic model for the interface shear strength between granular soil and structure considering surface morphology

Wei-Bin Chen [1], Wan-Huan Zhou [2]*, Łukasz Sadowski [3], and Zhen-Yu Yin [4]

[1] Ph.D. Candidate, State Key Laboratory of Internet of Things for Smart City and Department of Civil and Environmental Engineering, University of Macau, Macau, People's Republic of China. Email: YB77415@um.edu.mo

[2] Associate professor, State Key Laboratory of Internet of Things for Smart City and Department of Civil and Environmental Engineering, University of Macau, Macau, People's Republic of China (corresponding author). Email: hannahzhou@um.edu.mo

[3] Associate professor, Department of Building Engineering, Wroclaw University of Science and Technology, Wybrzeze Wyspianskiego 27, 50-370 Wroclaw, Poland. Email: lukasz.sadowski@pwr.edu.pl

[4] Associate Professor, Department of Civil and Environmental Engineering, The Hong Kong Polytechnic University, Hung Hom, Kowloon, Hong Kong, China. https://orcid.org/0000-0003-4154-7304. Email: zhenyu.yin@polyu.edu.hk

Metaheuristic model for the interface shear strength between granular soil and structure considering surface morphology

Abstract: A complete set of 13 morphological parameters in accordance with standard ISO 4287 was applied to quantifying a series of random profiles. These profiles were imported into a discrete numerical model to perform 480 interface shear tests on coarse-grained soils. The relevant morphological parameters were selected using Spearman's rank correlation coefficient for model selection. An optimal metaheuristic model was developed using a genetic algorithm and was further compared with the existing predicted formulas. The 2D discrete element method (DEM) results indicate that the highest correlation with shear strength was obtained for the hybrid parameter Pdq which represents not only the amplitude information but also the surface slope information on a random surface. The optimal model with one significant input variable (Pdq) was effectively selected through the Bayesian nonparametric general regression analysis. For irregular interface shearing widely existing in most geotechnical engineering, Pdq is more efficient and accurate to quantify the surface morphology or estimate the interface shear strength compared with relative roughness.

Keywords: Random surface; morphology; soil-structure interface; shear strength; metaheuristic model

Graphical abstract:

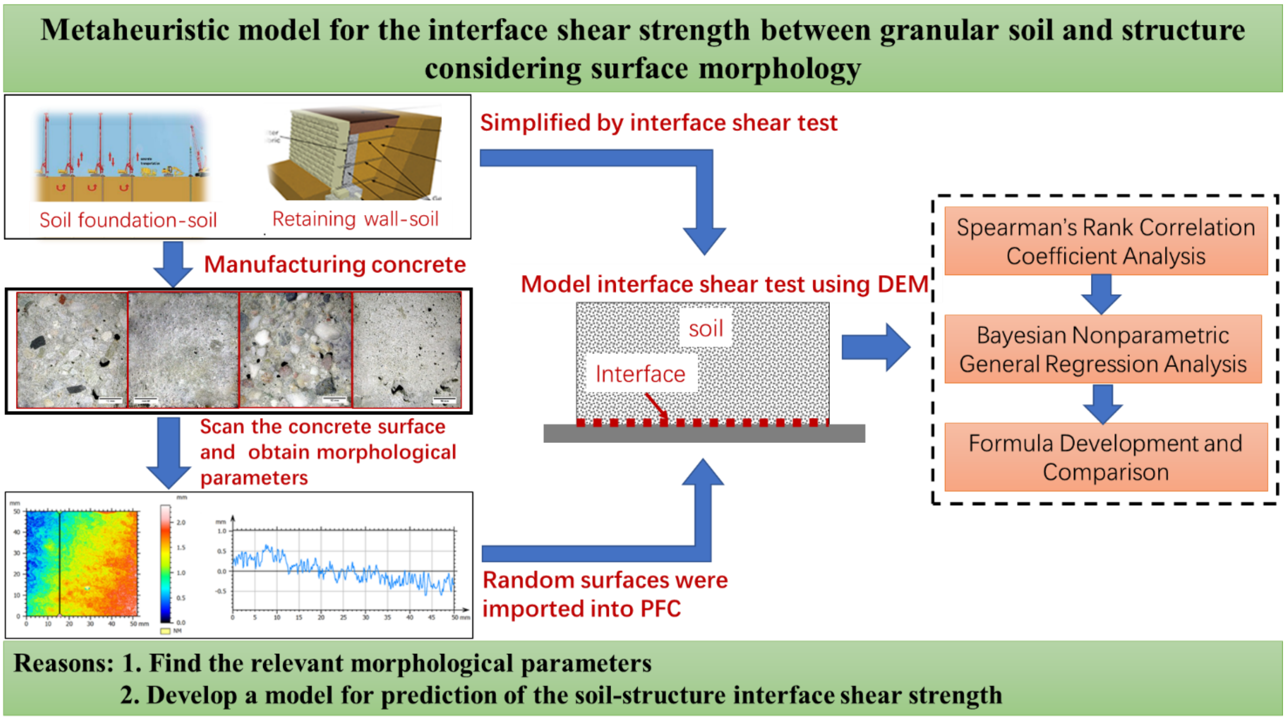

1. Introduction

Soil-structure systems, as shown in Fig. 1., including pile foundation-soil contact, retaining wall-soil interaction, and stabilizing piles in a slope, commonly exist in geotechnical engineering. These interactions can be regarded as a composite system. The connection between these two objects is the interface, which consists of the surface of the human-made construction and the surrounding granular material. Frictional resistance at the interface develops when the failure of the composite system occurs, leading to relative displacements at the interface (Chen et al., 2019; Chen et al., 2015; Wang et al., 2019b; Zhao et al., 2016; Zhou et al., 2012). Accurate evaluation of the interface shear strength is necessary to improve soil-structure interaction model development.

Various studies have shown that the soil-structure interface shear strength is influenced by the initial soil density (DeJong and Westgate, 2009; Oumarou and Evgin, 2005; Pra-ai and Boulon, 2017), particle geometry (DeJong and Westgate, 2009; DeJong et al., 2006; Dove et al., 2006; Frost et al., 2012; Vangla and Latha, 2015; Zhou et al., 2019), and particle grading (Liang et al., 2017; Wang et al., 2019a). The main consistent results showed that (a) the interface friction angle is greater for sands with more angular or elongated particle shapes; (b) both shear stress and dilatancy increase with relative density; and (c) the sample with a lower coefficient of uniformity presents higher shear stress and more pronounced dilative behavior. In addition, the experimental conditions have significant influences on the soil-structure interface strength. A multifunctional interface shear test apparatus was designed and fabricated to model soil–pile interactions under different boundary conditions (Evgin and Fakharian, 1997; Lehane and White, 2005; Wang et al., 2017), providing a more rational and economical design parameters for pile foundations. In terms of the role of temperature, the studies conducted by Di Donna and Laloui (2013); Di Donna et al. (2016); Yavari et al. (2016) demonstrated that the direct effect of temperature on the interface strength is negligible.

Apart from soil properties and experimental conditions, surface morphology is one of the structural properties and the effect of surface morphology on the mechanism of interaction between the granular assembly and the solid surface under numerical and experimental interface-shearing tests has been underlined repeatedly in previous studies, as summarized in Table 1. Among these studies, the surfaces used to be simplified or considered to be regular surfaces, i.e., saw-teeth or semi-arch pattern, for convenience of analysis. In addition, roughness was evaluated only qualitatively in several previous studies (Junaideen et al., 2004; Sharma et al., 2017). The surface morphology was approximately classified from very smooth to very rough through the observation of surface morphology. The disadvantage of this approach is the subjective results. Even though the approach of surface morphology quantification was adopted in most previous studies, the surface roughness has been quantified as one parameter. The most commonly used parameter was the relative roughness ($R_n = R_{max}/D_{50}$, where R_{max} is the maximum height of the surface and D_{50} is the average particle diameter) as proposed by Uesugi and Kishida (1986a, b). However, R_n fails to reflect the local distribution and partial variation of the surface profile. Obviously, the same R_n can be presented using many various profiles, as shown in Fig. 2. As shown in Table 1, some researchers have performed tests on non-random surfaces and have indicated that it is insufficient to adopt R_n to quantify the surface roughness. Accordingly, more comprehensive roughness parameters were introduced to describe the asperity characteristics (Dove and Jarrett, 2002; Guo et al., 2020; Rui et al., 2020; Wang et al., 2019d; Wu and Yang, 2016). Some results showed that these non-random surfaces can yield a higher interface shear strength than pure soil (Guo et al., 2020; Wu and Yang, 2016). In addition, given that most of structure surfaces are normally irregular or extremely random, the regular surface may fail to reflect the true behavior of an irregular interface. Several studies have focused on random surface shearing (Canakci et al., 2016; Han et al., 2018; Martinez and Frost, 2017; Rui et al., 2020), which provides a valuable understanding of the interface shear behavior. However, the current parameters may fail to satisfy the roughness quantification of the real surface due to its complexity, and the role of morphology parameters in the evaluation of interface shear strength under random surface shearing remains ambiguous.

To overcome limitations, the interaction between soil and random surfaces should be evaluated from the perspective of geotribology and more morphology parameters should be introduced, taking the local information and the spacing between peaks and valleys of the surface into consideration. The tribology theory has generally concentrated on the fields of wear, lubrication, surface characterization, and friction. Likewise, the theory can be applied to the investigation of the strength behavior of interface systems. Previous studies have proposed several techniques to quantify the surface morphology. Among these methods, the optical-based method (i.e. laser scanner device) was most widely used due to its high accuracy and fully non-destructive testing (Hoła et al., 2015; Sadowski and Mathia, 2016; Santos and Julio, 2007). The surface roughness can be characterized based on the scanned random surface and using a full quantitative approach. The 2D and 3D discrete element method (DEM) has been favorably adopted to address a range of geotechnical and geological issues, such as, soil-structure interactions (Chen et al.; Jing et al., 2018; Lai et al., 2016; Wang et al., 2007; Wang and Jiang, 2011; Wang et al., 2020; Zhu et al., 2019) and geological hazards (Shen et al., 2019; Utili et al., 2015). The DEM can also provide an effective technique to simulate and reproduce the interaction between the random surface and soil (Wang and Jiang, 2011). Once the scanned random surface is obtained, it is imported into the DEM to conduct a numerical interface shear test. Therefore, the DEM will be used to model the random surface-soil interface shear test in the present study.

Considering the above, the present study focuses on selecting the morphology parameters of random surfaces for evaluating the soil-structure interface strength. A complete set of morphology parameters in accordance with standard ISO 4287 (ISO, 2009) was applied to quantifying a series of random profiles of concretes. Based on the 2D DEM simulation, 480 interface shear tests with random profiles were conducted on coarse-grained soils. The relevant morphology parameters were selected using the Spearman's rank correlation coefficient for model selection. In addition, an optimal metaheuristic model was developed using a genetic algorithm and was further expressed by a formula. The proposed formula was compared with the existing predicted formulas.

2. Random Surface and Morphology Parameters

The investigated elements manufactured by Sadowski and Stefaniuk (2017) and Sadowski et al. (2018) consisted of an overlay and a substrate. The components of the concrete used to make the substrate are listed in Table 2. When the concrete substrates were maintained for 28 days, the specimens were fabricated to diversify the surface morphology. Four various surface treatment techniques were utilized to obtain four various concrete surface morphologies. The first type of surface was named by T1-raw, which was subjected to the special treatment, but was only grabbed. In practice, this is the most commonly used method. The second method (i.e., T2-as cast) was fabricated after contact with the manufactured formwork. Mechanical treatment was applied to the third type of surface (i.e., T3-ground) based on a portable angle grinder with an abrasive cutter and dust removal. After the dust was removed from the fourth type of surface (i.e., T4-shotblasted), T4 was continuously shotblasted by means of a lightweight shotblasting device. After treatments, a developed device based on the 3D triangulation scanner was used to scan the concrete surfaces and more details were presented by Sadowski et al. (2018). The scanning results showed a 3D isometric view of the investigated concrete surface morphology.

In this study, a total of 240 profiles were extracted from the four different concrete surfaces, with each concrete surface having 60 profiles. The isometric views of four different concrete surfaces and one of their corresponding profiles in the software MountainsMap (Map, 2014) are shown in Fig. 3. These profiles were analyzed in MountainsMap to obtain the values of the morphology parameters for surface characterization. The surface morphology parameters used were obtained according to standard ISO 4287 (ISO, 2009). The standard ISO 4287 contains five types of parameters, namely, amplitude parameter, spacing parameter, hybrid parameter, material ratio curves and related parameter, and peak count parameter. Each parameter is carefully presented in Table 3. The physical meaning of each parameter was explained by comparing the characteristics of profiles, as shown in Fig. 3. Except for amplitude parameters Psk and Pku, the remaining amplitude parameters are more common and easily calculated from the profiles. Profile P1 extracted from T1 has fairly deep valleys and scratches, which makes Psk negative, while the rest of the profiles have fairly high spikes or peaks, leading to the result that the Psk is positive. Profiles possessing comparatively few low valleys and high peaks lead to a Pku of less than 3, whereas profiles with many low valleys and high peaks are reflected in a Pku of more than 3. Clearly, P1 with a Pku of less than 3 has fewer low valleys and high peaks than the other profiles, and the other three with a Pku of more than 3 have a high density of low valleys and high peaks. Pdq describes the root mean square for the local slope of the profile, which is presented as degree in the present study. Overall, the local slope of P1 is most stable, while the local slope of P4 is steepest. Accordingly, P1 has the smallest Pdq and the largest Pdq is for P4. Evidently, from P1 to P4, the density of the peak gradually increases and the corresponding PPc increases. Conversely, the Psm decreases because the distance between neighboring peak-valley gradually becomes narrow from P1 to P4. The difference in Pmr and Pdc for these four profiles can be easily read from the profiles.

3. Numerical Simulation of Interface Shear Test

3.1. 2D DEM simulation limitations

It is accepted that 2D DEM has the following limitations in terms of modeling the behavior of soils. First, the void ratio and porosity values achieved in a 2D model are much smaller than those in a 3D model. Second, the dilation in the 2D model can be much higher than that in the 3D model since the 2D plane assembly can only dilate due to the removal of freedom in the cross-plane direction. These differences may lead to overestimation of both the interface shear stress and the volumetric deformation when conducting 2D numerical interface shear tests. Despite these limitations, the 2D DEM was also used to simulate soil behavior and soil-structure behavior due to high computational efficiency, as mentioned above. In the present study, the numerical simulation was conducted with a 2D-particle flow code (PFC^{2D}), based on the DEM developed by Itasca (2008).

3.2. Numerical model and model process

To compensate for the interlocking influence induced by the various shapes of particles, a rolling resistance linear contact model was applied to contacts (Iwashita and Oda, 1998). The test apparatus, with length of 90 mm and height of 25 mm, is comprised of an upper rigid shear box filled with particles and a rigid lower boundary. The latter one consists of a random surface and two smooth walls of auxiliary zones" of 20 mmat each end of the shear box to eliminate the boundary effect. The random surfaces imported into PFC^{2D} were obtained from the profiles of concrete surfaces. There is no particle-to-bottom boundary friction within the auxiliary zones. The concrete surface will suffer some damage and abrasion during shearing and the corresponding morphology of post shearing surface would change if we investigate this issue using laboratory tests. However, numerical simulation will avoid damage and abrasion on the imported random surface because the random surface is assumed to be stiff or nondeformable in PFC^{2D}. The numerical simulation model is shown in Fig. 4. The technique of specimen generation called particle size growing proposed by Chareyre and Villard (2002) was adopted to obtain a relatively isotropic specimen. Specifically, based on a particle size distribution, a series of particles with a certain diameter range was seeded inside the shear box and their sizes gradually grew. This particle size growing process stopped when the normal pressure applied on the top boundary achieved the targeted value. The radii of particles in the specimen were fixed in the process of shearing. The sample was verified to be uniform at the beginning of the shear phase by checking the spatial distributions of the force chains and void ratio. The bottom random surface started moving horizontally in the x-direction by applying a velocity of 1.0×10^{-3} m/min recommended by ASTM D5321 to fulfill a quasistatic interface shearing. A constant normal pressure applied on the moveable top wall was sustained by a built-in servo control system in PFC^{2D}, while the two lateral counterparts were fixed throughout shearing.

The shearing behavior was obtained by recording the displacements and forces on the walls. The shear stress ratio is the ratio of shear stress to normal stress. The normalized shear displacement is defined as the ratio of shear displacement to D_{50}. The input parameters follow the numerical 2D interface shear test conducted by Zhu et al. (2017), as demonstrated in Table 4. The effect of normal stress on interface shearing behavior in preliminary tests is shown in Fig. 5. The peak shear stress is shown to increase with the normal stress. The specimens dilate with a decreasing rate and the degree of dilatancy decreases with increasing normal stress. All the preliminary results are consistent with the previous numerical and experimental results (Gu et al., 2017; Guo et al., 2020; Jing et al., 2018; Wang et al., 2019d).

3.3. Numerical test schemes

To increase the database, three different mean particle sizes, i.e., D_{50} = 0.35 mm, D_{50} = 0.53 mm, and D_{50} = 0.80 mm, but the same uniformity coefficient were adopted for the interface shear test. The detailed three particle size distributions (PSD1, PSD2, and PSD3) are demonstrated in Fig. 6. Each specimen for the three different mean particle sizes contains 4,444, 10,000, and 22,500 particles. Accordingly, a total of 480 simulated interface shear tests with random surfaces were sheared under a normal stress of 100 kPa, as shown in Table 5. The initial void ratios of the specimens range from 0.182 to 0.184. Direct shear tests on the specimen with varying mean diameters were also conducted, to obtain the shear strength of each soil. The normalized interface stress was designated by the efficiency parameter (IE), which was proposed by Koerner (2012). IE is the ratio of $tan\delta$ to $tan\varphi$, where $tan\delta$ presents the interface friction coefficient, whereas $tan\varphi$ is the friction coefficient of pure soil. The efficiency at the peak state IE_P can be calculated using the peak friction coefficients of the interface and pure soil. The value of the efficiency parameter ranges from 0.0 (small interface strength) to 1.0 (fully mobilized soil strength).

3.4. **Typical interface shearing behavior**

Four typical macroscopic interface shearing behaviors versus normalized shear displacement are illustrated in Fig. 7. The general curve trend shows that a post-peak strain softening to steady state because of the low initial void ratio. Continuous dilation is also observed in Fig. 7(b). Similar curves were also observed from the results of other interface shear tests with different surface geometries, but their corresponding curves are not shown. The peak interface efficiency of each simulation IE_P was collected for further analysis using Spearman's rank correlation coefficient and by developing metaheuristic relationships between peak interface efficiency and surface morphology parameters.

4. Results and Discussion

The analysis of Spearman's rank correlation coefficient was conducted to eliminate the irrelevant morphology parameters with the peak interface efficiency IE_P. Furthermore, the relevant morphology parameters were combined to form the potential models in the process of model selection. The optimal model was selected among the potential models based on the result of Bayesian nonparametric general regression. The obtained optimal model was formulated and validated with previous studies.

4.1. Analysis of correlation by means of Spearman's rank correlation coefficient

Compared with the Pearson product-moment correlation, Spearman's rank-order correlation belongs to the nonparametric analysis. Spearman's rank correlation coefficient, ρ_S, presents the degree and direction of dependence between two ranked variables. Because ρ_S is only mildly sensitive to divergent results, it is especially effective in analyzing the data where the distribution does not follow the normal distribution. According to Kowalczyk et al. (2004), the two random variables x and y in the analysis of Spearman's rank correlation coefficient can be obtained from the following equation:

$$\rho_S = corr \cdot (f(x)_x, f(y)_y) \qquad (1)$$

where $corr$ is the Pearson correlation coefficient; $f(x)_x$ is the distribution function of variable x at point x, while $f(y)_y$ is the distribution function of variable y at point y. The value of ρ_S ranges from -1 to 1. Kowalczyk et al. (2004) also assumed that the data investigated are appropriate to perform an artificial neural network analysis, when the values of ρ_S range from either -1 to -0.4 or from 0.4 to 1.

In this part, the correlation between peak interface efficiency IE_P and 13 morphology parameters was determined using the Spearman's rank correlation coefficient. The parameters with length units were normalized by average diameter D_{50}. The statistics of 13 morphology parameters and peak interface efficiency IE_P based on the results of 480 interface shear tests are presented in Table 6. The correlations between the 13 morphology parameters and IE_P with the calculated values of ρ_s are shown in Table 7. From Table 7, it appears that ρ_s is in a range of 0.4 to 1 or -1 to -0.4 for parameters Pp/D_{50}, Pv/D_{50}, Pz/D_{50}, Pc/D_{50}, Pa/D_{50}, Pq/D_{50}, Psm/D_{50}, Pdq, Pdc/D_{50} and PPc, indicating the highest value (0.777) for parameter Pdq. A positive ρ_s indicates an increase in the values of the parameter with the increase of IE_P,whereas a negative ρ_s indicates a decrease in the values of the parameter with IE_P increased. The rotation and translation of granular material over the random surface are affected by the surface morphology, which indirectly influences the mobilized efficiency of soil. The hybrid parameter Pdq includes not only the amplitude information but also the surface slope information on a random surface; therefore, its effect on IE_P is most productive. PPc signifies the peak number per unit length of a profile and is able to positively affect the soil movement over an interface. More peaks per unit length will lead to decreasing the distance between neighboring peak-valley pairs in a profile, which indicates that PPc is inversely proportional to PSm. Accordingly, the value of ρ_s for PSm/D_{50} is negative and IE_P has a negative relationship with PSm/D_{50}. The ρ_s is less than 0.4 for the remaining parameters, which suggesting that the correlation between the remaining parameters and IE_P is insignificant. As presented in Table 3, Psk is used to express the symmetry of peaks and valleys, while Pku is utilized to describe the sharpness of a surface. Both parameters are normally used for the evaluation of gloss and luster, but not for the evaluation of frictional force (Olympus, 2014; Vik et al., 2014). Given all that, the ten parameters p/D_{50}, Pv/D_{50}, Pz/D_{50}, Pc/D_{50}, Pa/D_{50}, Pq/D_{50}, Psm/D_{50}, Pdq, Pdc/D_{50}, and PPc are the relevant input variables for metaheuristic model development.

4.2. Data description and model selection

A total of 480 databases were prepared for analysis based on the Bayesian nonparametric general regression (BNGR) carefully presented in Appendix A. The ten selected morphology parameters were used to establish a metaheuristic model to estimate the peak interface efficiency IE_P. The parameters, i.e., Pp/D_{50}, Pv/D_{50}, Pz/D_{50}, Pc/D_{50}, Pa/D_{50}, Pq/D_{50}, Psm/D_{50}, Pdq, Pdc/D_{50}, and PPc, are designated as x_1, x_2, x_3, x_4, x_5, x_6, x_7, x_8, x_9, and x_{10}, respectively.

The traditional regression approaches have an obvious weakness that a large number of the model candidates are generated due to a large number of combinations of potential function structures from the same set of input variables. However, the BNGR method vanquishes this disadvantage from traditional methods. Based on the BNGR algorithm descripted in Appendix A, $2^{10}- 1$ =1023 models were generated as the potential models. Because the prior distribution choice for the vector θ was independent of the model selection (Yuen et al., 2016), both the perdition error scale parameter and the smoothing scale parameter were analyzed based on the uniform prior distributions of [0, 100]. According to the current database, 70% of the database (336 points) was randomly selected as the training database which was used to obtain the optimal model while the remaining 30% of the database (144 points) was used for verification of the selected models. Based on the training database, the smoothing scale parameter was calculated by Eq. (11),whereas the perdition error scale parameter was measured using Eq. (12). The results of some selected models using BNGR algorithm are carefully summarized in Table 8. The first column represents the selected input variables and the sixth column shows the plausibility of the corresponding model, which is ranked in order. According to the value of plausibility, model (x_8) is the optimal model. Fig. 8 demonstrates that the optimal model shows a high fitting capability in the training phase, which means that it has an efficient learning ability. The most plausible model (x_8) is made of the hybrid parameter, Pdq. Pdq is a combination of amplitude and spacing information of surface and has been proven to be most relevant to IE_P according to the Spearman's rank correlation coefficient analysis.

4.3. Optimal model validation

In this section, the remaining 30% of the database (144 points) was used for verification of the optimal model. Fig. 9 shows the measured peak interface efficiency IE_P from the remaining 30% of the database versus the predicted IE_P with the perfect matched line, i.e., the 45° line. All the prediction results based on the optimal model and the other six models (listed in Table 8) are plotted in this figure. The selected optimal model possesses the highest prediction capability based on the least number of morphology parameters compared with those for the models with the two input variable combinations (x_8 combined with the other six parameters). Fig. 10 shows that the full model (i.e., model with all input variables (x_1, x_2, x_3, x_4, x_5, x_6 x_7, x_8, x_9 and x_{10}) has a lower fitting capacity than that for optimal model, indicating that some input parameters are redundant for metaheuristic model development and cannot increase the fitting capacity but instead decrease the accuracy of model prediction.

In previous studies, the most commonly used parameter for the description of surface morphology was the relative roughness $R_n = R_{max}/D_{50}$ (i.e., Pz/D_{50} in this study). The model with R_n or Pz/D_{50} was also used to predict IE_P. Fig. 11 shows that the models with R_n or Pz/D_{50} has a much lower predictive capacity than that for optimal model. Because the input variable R_n can only represent the local maximum height of the surface, the precited points disperse in a larger domain compared to the distribution of precited points for the optimal model.

For a more objective comparison, two traditional indicators, the mean absolute relative error (MARE) and mean absolute error (MAE), were calculated for the comparison of predictive capability among all selected models, as shown in Table 9. Compared with the other models, the optimal model has the smallest values of both MAE and MARE. Through the above comparisons, the model (x_8) was verified to be optimal for the prediction of IE_P.

4.4. Predicted formula development and comparison with existing predicted formulas

The most plausible model (x_8) is made of the hybrid parameter, Pdq. For the convenience of engineering applicability, the optimal model (x_8) was further expressed by a formula. By incorporating the observations of the relationship between Pdq and peak interface efficiency IE_P, the optimal model class for estimation of IE_P is proposed as follows

$$IE_P = a + Pdq * b \quad (2)$$

where a and b are all obtained from curve fitting. Seventy percent of the database was used to develop the predicted formula based on the hybrid parameter, Pdq. Fig. 12 shows the learning capability of the proposed formula and its expression. Fig. 13 shows the measured IE_P from the remaining 30% of the database versus the calculated IE_P from the proposed formula as well as the perfect matched line.

As mentioned in section 4.3, the most commonly used parameter for estimation of interface strength is the relative roughness R_n in previous studies. In the present study, the relationship between R_n and the peak shear stress ratio is plotted in Fig. 14(a). To verify the findings of the present study, several relevant existing studies (DeJong and Westgate, 2009; Jing et al., 2018; Sharma et al., 2019; Su et al., 2018; Subba Rao et al., 1998; Uesugi and Kishida, 1986b; Zhou et al., 2007) have been selected for comparison, as shown in Fig. 14(b). As reported by Su et al. (2018), the peak shear stress ratio remains nearly constant as R_n is more than approximately 0.25, while the critical value was reported to be approximately 0.375 by Jing et al. (2018). For the other studies, generally, the peak stress ratio increases with R_n when R_n is less than 1.0, which is consistent with the findings of the current study. Among previous studies, the most commonly used pattern of the existing predicted formula based on R_n contains the exponential function, the polynomial function, and the hyperbolic function. Seventy percent of the database was used to obtain the expressions of these three functional patterns. Fig. 15 shows the learning capabilities of these three expressions. The remaining 30% of the database was used to show the predictive capability of these three expressions, as shown in Fig. 16.

Compared with the three existing predicted formulas, the proposed model has a higher learning capability in the training phase and higher predictive ability in the testing phase because the proposed model in both the training phase and testing phase has a higher coefficient of determination R^2. This fact was also verified by the results of Table 10, showing that both the lowest MAE and MARE are found for the proposed formula. The observations indicate that for irregular interface shearing existing in the most geotechnical engineering, using R_n for characterizing surface morphology and estimation of IE_P is inadequate but hybrid parameter Pdq is more efficient and accurate to estimate IE_P, instead, explained as follows. R_n, as the local morphology parameter of an interface, is only evaluated by the maximum height of a profile. It will be efficient for the morphology evaluation of regular surfaces but not for the morphology evaluation of random surfaces. Pdq, as a global morphology parameter of an interface, provides not only height information but also spacing information along the full investigated profile. Accordingly, it is more efficient to evaluate the interface strength. It may be noted that the conclusion was reached based on the 2D DEM simulation, and widespread application needs to conduct more 3D numerical and experimental investigations.

5. Conclusion

Based on the 2D DEM simulation, 480 interface shear tests with random profiles were conducted on coarse-grained soils. The relevant morphology parameters were selected using Spearman's rank correlation coefficient. BNGR was applied to forming a metaheuristic model for estimation of the soil-structure interface shear strength. The key observations are summarized as follows:

(1) ρ_s is in a range of 0.4 to 1 or -1 to -0.4 for parameters Pp/D_{50}, Pv/D_{50}, Pz/D_{50}, Pc/D_{50}, Pa/D_{50}, Pq/D_{50}, Psm/D_{50}, Pdq, Pdc/D_{50} and PPc. The highest Spearman's rank coefficient, amounting to 0.788, has been obtained for hybrid parameter Pdq which represents not only the amplitude information but also the surface slope information on a random surface.

(2) One significant input variable (Pdq) was effectively selected from 10 potential candidates (Pp/D_{50}, Pv/D_{50}, Pz/D_{50}, Pc/D_{50}, Pa/D_{50}, Pq/D_{50}, Psm/D_{50}, Pdq, Pdc/D_{50} and PPc) by using the BNGR algorithm. The optimal model selected was verified on the testing data and compared with the prediction results of some selected models, the full model, and the model with the most commonly used parameter.

(3) Based on the 2D DEM results, the proposed formula was compared with the existing predicted formulas. For irregular interface shearing, using R_n for characterizing surface morphology and

estimating IE_P is inadequate, but the hybrid parameter Pdq is more efficient and accurate for estimating IE_P.

It is noteworthy that the results were achieved based on the 2D DEM simulation, which has inherent limitations in investigating real 3D problems. The granular soil was modeled with circular disks in this study and the rolling resistance was adopted to compensate for the lack of angularity of circular particles. The simplifications in this study surely cause differences between the real and DEM investigations, and 2D numerical investigations still provide helpful results to illustrate the correlation between morphology parameters and interface shear strength. To make the conclusions broad, 3D DEM simulations will be the future work.

Acknowledgements

The authors wish to thank the support funded by The Science and Technology Development Fund, Macau SAR (File no. 0025/2020/ASC, SKL-IOTSC-2018-2020, 0035/2019/A1, and 193/2017/A3), The Ministry of Science and Technology of the People's Republic of China (Grant No. 2019YFB1600700), The Guangdong Provincial Department of Science and Technology (Grant No. 2019B111106001), The Fundo para o Desenvolvimento das Ciencias e da Tecnologia ((Grant No. 0026/2020/AFJ), and The GRF project (Grant No. 15217220) from the Research Grants Council (RGC) of Hong Kong, and The National Natural Science Foundation of China (Grant No. 52022001).

Appendix A

Since Yuen and Ortiz (2016) developed an innovative Bayesian nonparametric general regression (BNGR) algorithm, BNGR has been applied to addressing the engineering issues (Zhao et al., 2019). Compared with the traditional generalized regression method, two merits of the BNGR method have been proven. Specifically, the prior distribution of the regression coefficients is independent of model selection. In addition, the number of model candidates is decreased significantly.

Based on the generalized regression neural network (GRNN), the regression relationship between the input variables (denoted by vector, X) and output variable y is obtained without presetting a specific parametric equation. Thus, the output y can be expressed as follows:

$$E(y|X)=\frac{\int_{-\infty}^{\infty} yp(X,y)dy}{\int_{-\infty}^{\infty} p(X,y)dy} \tag{3}$$

where $p(X,y)$ represents the joint probability density function (PDF) of X and y.

Considering the unknown $p(X,y)$ for most conditions, the kernel density approximation $\hat{p}(X,y)$ is used to compute it. The Gaussian mixture distribution is normally chosen to address it, as shown in the following equation:

$$\hat{p}(X,y)=\frac{1}{N(2\pi\sigma_1^2)^{(d+1)/2}}\sum_{n=1}^{N} exp\left[-\frac{(X-X_n)^T(X-X_n)+(y-y_n)^2}{2\sigma_1^2}\right] \tag{4}$$

where σ_1^2, an unknown parameter, is adopted to balance the regression model smoothness and the fitting capability. Substituting Eq. (3) into Eq. (4), we can obtain the expected value of y expressed by:

$$\hat{y}(X)=E_{\hat{p}}(y|X)=\frac{\sum_{n=1}^{N} y_n\, exp[-(X-X_n)^T(X-X_n)/(2\sigma_1^2)]}{\sum_{n=1}^{N} exp[-(X-X_n)^T(X-X_n)/(2\sigma_1^2)]} \tag{5}$$

To avoid the over-fitting and select the proper value of σ_1^2, the predicted point is eliminated by summing Eq. (5), Eq. (5) transforms into:

$$\hat{y}(X_m)=\frac{\sum_{\substack{n=1\\ n\neq m}}^{N} y_n\, exp[-(X_m-X_n)^T(X_m-X_n)/(2\sigma_1^2)]}{\sum_{\substack{n=1\\ n\neq m}}^{N} exp[-(X_m-X_n)^T(X_m-X_n)/(2\sigma_1^2)]} \tag{6}$$

Thus, by fitting the predicted data obtained from Eq. (6) with the measured data, we can obtain the optimum value of σ_1^2.

Based on nonparametric regression, GRNN represents an improved method in the neural networks. However, it is not objective to choose which input variable has great influences on the output. The subjectivity of human beings can be avoided by Bayesian inference because Bayesian inference uses an objective approach to select the significance of each input variable based on the measured data. Accordingly, taking advantage of Bayesian inference, it is conceivable to couple GRNN with Bayesian inference to determine the implied input variables.

For the GRNN, there is an unknown parameter, σ_1^2. It can be obtained from Eq. (6). Likewise, an unknown vector, θ, exists in the Bayesian General Regression. Based on Bayes' principle, the posterior PDF of θ is defined as:

$$p(\theta|y, X, C) = \frac{p(y|\theta, X, C)p(\theta|C)}{p(y|X, C)} \tag{7}$$

where C and $p(y|X, C())$ are the general regression model and the normalizing constant, respectively. The prior PDF of the uncertain parameters, $p(\theta|C)$, is adopted to reflect the prior knowledge of the consciousness of the researchers. The likelihood function, $p(y \mid \theta, X, C)$, is used to represent the fitting capability of the measured data given the parameter vector, θ.

To calculate the likelihood function in Eq. (7), the equation can be transformed into the form of conditional PDF as:

$$p(y|\theta, X, C) = \prod_{m=1}^{N} p(y_m|y_1, \cdots, y_{m-2}, y_{m-1}, \theta, X, C) \tag{8}$$

where

$$p(y_m|y_1, \cdots, y_{m-2}, y_{m-1}, \theta, X, C) = \left(2\pi\sigma_{2,m}^2\right)^{-1/2} exp\left[-\frac{\left(y_m - \hat{y}_{m|m-1}(X_m)\right)^2}{2\sigma_{2,m}^2}\right] \tag{9}$$

where $\hat{y}_{m|m-1}(X_m)$ is the regression of y on X in accordance with the first m-1 measured data point, obtained as:

$$\hat{y}_{m|m-1}(X_m) = \frac{\sum_{n=1}^{m-1} y_n \, exp\left[-\left((X_m-X_n)^T(X_m-X_n)\right)/2\sigma_{1,m}^2\right]}{\sum_{n=1}^{m-1} exp\left[-\left((X_m-X_n)^T(X_m-X_n)\right)/2\sigma_{1,m}^2\right]} \tag{10}$$

$$\sigma_{1,m}^2 = \frac{v_1}{m-1}\sum_{n=1}^{m-1}(X_m - X_n)^T(X_m - X_n) \tag{11}$$

$$\sigma_{2,m}^2 = \frac{v_2}{\sum_{n=1}^{m-1} exp[-2(X_m-X_n)^T(X_m-X_n)]} \tag{12}$$

where v_1 is the smoothing scale parameter and v_2 is the prediction error scale parameter. Both parameters can be obtained (Yuen and Ortiz, 2016).

To date, the unknown vector, $\theta = [v_1 \quad v_2]$, has been expressed based on the framework of the BNGR approach. Thus, the posterior PDF of θ can be written as:

$$p(v_1, v_2 | \, y, X\,, C) \propto p(v_1, v_2)p(y|v_1, v_2, X, C)$$

$$\propto (v_2)^{-(N/2)} \times exp\left[-\frac{1}{2v_2}\sum_{m=1}^{N} \Omega_m \left(y_m - \hat{y}_{m|m-1,v_1}(X_m)\right)^2\right] \tag{13}$$

where Ω_m is defined as:

$$\Omega_m = \sum_{n=1}^{m-1} exp[-2(X_m - X_n)^T(X_m - X_n)] \tag{14}$$

Given that the derivative of the posterior PDF versus the parameter, v_2, is equal to zero, as follows:

$$\frac{\partial p(v_1,v_2|y,X,C)}{\partial v_2} = 0 \tag{15}$$

then,

$$v_2^*(v_1) = \frac{1}{N}\sum_{m=1}^{N} \Omega_m \left(y_m - \hat{y}_{m|m-1,v_1}(X_m)\right)^2 \tag{16}$$

By maximizing the following function, the parameter, v_1^*, can be calculated:

$$g(v_1) = p(v_1, v_2^*(v_1)|y, X, C) \tag{17}$$

According to the calculated θ, the regression model is expressed by the relationship between a subset of potential input variables and the interested output. The suitable set of design variables can be obtained from the optional models using the Bayesian inference theorem, as presented in the following. Various combinations of these potential input variables generate various regression models, such as $C^{(1)}$, $C^{(2)}$, …, $C^{(3)}$.

Given Bayes's theorem, the plausibility of a model can be obtained as:

$$P\left(C^{(k)}|y,X\right)=\frac{p\left(y|X,C^{(k)}\right)P\left(C^{(k)}\right)}{\sum_{k=1}^{N_C}p\left(y|X,C^{(k)}\right)P\left(C^{(k)}\right)} \tag{18}$$

Finally, $p\left(y\mid X,C^{(k)}\right)$can be readily obtained:

$$p\left(y|X,C^{(k)}\right)\approx\frac{2\Gamma(N/2+1)\sqrt{2\pi\prod_{m=1}^{N}(\Omega_m/|\hbar_k(v_1^*)|)}}{(B_{U1}-B_{L1})(B_{U2}-B_{L2})\pi^{N/2}}$$

$$\times\left[\sum_{m=1}^{N}\Omega_m\left(y_m-\hat{y}_{m|m-1,v_1}(X_m)\right)^2\right]^{-(N/2+1)} \tag{19}$$

The framework of Bayesian combined with GRNN was presented. It is noteworthy that, with the same group of input variables, the function form is automatically produced based on GRNN's theorem. Thus, it is very efficient to conduct Bayesian model selection because it is unnecessary to produce various function structures using the same group of input variables compared with the conventional generalized regression method.

References

Canakci, H., Hamed, M., Celik, F., Sidik, W., Eviz, F., 2016. Friction characteristics of organic soil with construction materials. Soils Found. 56, 965-972.

Chareyre, B., Villard, P., 2002. Discrete element modeling of curved geosynthetic anchorages with known macro-properties, Proc., First Int. PFC Symposium, pp. 197-203.

Chen, W.-B., Xu, T., Zhou, W.-H., Microanalysis of smooth Geomembrane–Sand interface using FDM–DEM coupling simulation. Geotext. Geomembranes. 49, 276-288.

Chen, W.-B., Zhou, W.-H., dos Santos, J.A., 2020. Analysis of consistent soil–structure interface response in multi–directional shear tests by discrete element modeling. Transp. Geotech. 24, 100379.

Chen, W.-B., Zhou, W.-H., Jing, X.-Y., 2019. Modeling Geogrid Pullout Behavior in Sand Using Discrete-Element Method and Effect of Tensile Stiffness. Int. J. Geomech. 19, 04019039.

Chen, X., Zhang, J., Xiao, Y., Li, J., 2015. Effect of roughness on shear behavior of red clay–concrete interface in large-scale direct shear tests. Can. Geotech. J. 52, 1122-1135.

Chu, L.-M., Yin, J.-H., 2005. Comparison of interface shear strength of soil nails measured by both direct shear box tests and pullout tests. J. Geotech. Geoenviron. 131, 1097-1107.

DeJong, J.T., Westgate, Z.J., 2009. Role of initial state, material properties, and confinement condition on local and global soil-structure interface behavior. J. Geotech. Geoenviron. 135, 1646-1660.

DeJong, J.T., White, D.J., Randolph, M.F., 2006. Microscale observation and modeling of soil-structure interface behavior using particle image velocimetry. Soils Found. 46, 15-28.

Di Donna, A., Laloui, L., 2013. Advancements in the geotechnical design of energy piles, International EAGE Workshop on Geomechanics and Energy. European Association of Geoscientists & Eng., pp. cp-369-00009.

Di Donna, A., Loria, A.F.R., Laloui, L., 2016. Numerical study of the response of a group of energy piles under different combinations of thermo-mechanical loads. Comput. Geotech. 72, 126-142.

Dove, J., Bents, D., Wang, J., Gao, B., 2006. Particle-scale surface interactions of non-dilative interface systems. Geotext. Geomembranes. 24, 156-168.

Dove, J.E., Jarrett, J.B., 2002. Behavior of dilative sand interfaces in a geotribology framework. J. Geotech. Geoenviron. 128, 25-37.

Evgin, E., Fakharian, K., 1997. Effect of stress paths on the behaviour of sand steel interfaces. Can. Geotech. J. 33, 853-865.

Feng, S.-J., Liu, X., Chen, H.-X., Zhao, T., 2018. Micro-mechanical analysis of geomembrane-sand interactions using DEM. Comput. Geotech. 94, 58-71.

Frost, J.D., Kim, D., Lee, S.-W., 2012. Microscale geomembrane-granular material interactions. KSCE J. Civ. Eng. 16, 79-92.

Gu, X., Chen, Y., Huang, M., 2017. Critical state shear behavior of the soil-structure interface determined by discrete element modeling. Particuology. 35, 68-77.

Guo, J., Wang, X., Lei, S., Wang, R., Kou, H., Wei, D., 2020. Effects of groove feature on shear behavior of steel-sand interface. Adv. Civ. Eng. 2020. https://doi.org/10.1155/2020/9593187.

Han, F., Ganju, E., Salgado, R., Prezzi, M., 2018. Effects of interface roughness, particle geometry, and gradation on the sand–steel interface friction angle. J. Geotech. Geoenviron. 144, 04018096.

Hoła, J., Sadowski, Ł., Reiner, J., Stach, S., 2015. Usefulness of 3D surface roughness parameters for nondestructive evaluation of pull-off adhesion of concrete layers. Constr. Build Mater. 84, 111-120.

Hu, L., Pu, J., 2004. Testing and modeling of soil-structure interface. J. Geotech. Geoenviron. 130, 851-860.

ISO, E., 2009. 4287: 2009. Geometrical Product Specifications (GPS)-Surface texture: Profile method–Terms, definitions and surface texture parameters (ISO 4287: 1997+ Cor 1: 1998+ Cor 2: 2005+ Amd 1: 2009) (includes Corrigendum AC: 2008 and Amendment A1: 2009).

Itasca, P.D., 2008. Particle Flow Code in 3 Dimensions, User's Guide.

Iwashita, K., Oda, M., 1998. Rolling resistance at contacts in simulation of shear band development by DEM. J. Eng. Mech. 124, 285-292.

Jing, X.Y., Zhou, W.H., Zhu, H.X., Yin, Z.Y., Li, Y., 2018. Analysis of soil‐structural interface behavior using three‐dimensional DEM simulations. Int. J. Numer. Anal. Met. 42(2), 339-357.

Junaideen, S., Tham, L., Law, K., Lee, C., Yue, Z., 2004. Laboratory study of soil nail interaction in loose, completely decomposed granite. Can. Geotech. J. 41, 274-286.

Koerner, R.M., 2012. Designing with geosynthetics. Xlibris Corporation.

Kowalczyk, T., Pleszczynska, E., Ruland, F., 2004. Grade models and methods for data analysis: with applications for the analysis of data populations. Springer Science & Business Media.

Lai, H.-j., Zheng, J.-j., Zhang, R.-j., Cui, M.-j., 2016. Visualization of the formation and features of soil arching within a piled embankment by discrete element method simulation. J. Zhejiang Univ-Sc. A. 17, 803-817.

Lehane, B.M., White, D.J., 2005. Lateral stress changes and shaft friction for model displacement piles in sand. Can. Geotech. J. 42, 1039-1052.

Liang, Y., Yeh, T.-C.J., Wang, J., Liu, M., Hao, Y., 2017. Effect of particle size distribution on soil-steel interface shear behavior. Soil Mech. Found. Eng. 54, 310-317.

Map, M., 2014. Software (Digital Surf, Besançon, France).

Martinez, A., Frost, J., 2017. The influence of surface roughness form on the strength of sand–structure interfaces. Geotech. Lett. 7, 104-111.

Olympus, 2014. Roughness (2D) parameter. https://www.olympus-ims.com/en/metrology/surface-roughness-measurement-portal/parameters/.

Oumarou, T.A., Evgin, E., 2005. Cyclic behaviour of a sand steel plate interface. Can. Geotech. J. 42, 1695-1704.

Pra-ai, S., Boulon, M., 2017. Soil–structure cyclic direct shear tests: a new interpretation of the direct shear experiment and its application to a series of cyclic tests. Acta Geotech. 12, 107-127.

Rui, S., Wang, L., Guo, Z., Cheng, X., Wu, B., 2020. Monotonic behavior of interface shear between carbonate sands and steel. Acta Geotech. 1-21.

Sadowski, Ł., Mathia, T.G., 2016. Multi-scale metrology of concrete surface morphology: Fundamentals and specificity. Constr. Build Mater. 113, 613-621.

Sadowski, Ł., Stefaniuk, D., 2017. Microstructural evolution within the interphase between hardening overlay and existing concrete substrates. Applied Sciences 7, 123.

Sadowski, Ł., Żak, A., Hoła, J.J.A.o.C., Engineering, M., 2018. Multi-sensor evaluation of the concrete within the interlayer bond with regard to pull-off adhesion. Arch. Civ. Mech. Eng. 18, 573-582.

Santos, P.M., Julio, E.N., 2007. Correlation between concrete-to-concrete bond strength and the roughness of the substrate surface. Constr. Build Mater. 21, 1688-1695.

Sharma, M., Samanta, M., Punetha, P.J.I.J.o.G., 2019. Experimental investigation and modeling of pullout response of soil nails in cohesionless medium. Int. J. Geomech. 19, 04019002.

Sharma, M., Samanta, M., Sarkar, S., 2017. Laboratory study on pullout capacity of helical soil nail in cohesionless soil. Can. Geotech. J. 54, 1482-1495.

Shen, W., Zhao, T., Dai, F., Jiang, M., Zhou, G.G., 2019. DEM analyses of rock block shape effect on the response of rockfall impact against a soil buffering layer. Eng. Geol. 249, 60-70.

Su, L.-J., Zhou, W.-H., Chen, W.-B., Jie, X., 2018. Effects of relative roughness and mean particle size on the shear strength of sand-steel interface. Measurement 122, 339-346.

Subba Rao, K., RAO, K., ALLAM, M., ROBINSON, R.J.P.o.t.I.o.C.E.-G.E., 1998. Interfacial friction between sands and solid surfaces. Proceedings of the Institution of Civil Engineers-Geotechnical Engineering. 131, 75-82.

Uesugi, M., Kishida, H., 1986a. Frictional resistance at yield between dry sand and mild steel. Soils Found. 26, 139-149.

Uesugi, M., Kishida, H., 1986b. Influential factors of friction between steel and dry sands. Soils Found. 26, 33-46.

Utili, S., Zhao, T., Houlsby, G., 2015. 3D DEM investigation of granular column collapse: evaluation of debris motion and its destructive power. Eng. Geol. 186, 3-16.

Vangla, P., Latha, G.M., 2015. Influence of particle size on the friction and interfacial shear strength of sands of similar morphology. Int. J. Geosyn. Ground Eng. 1(1), 6.

Vik, M., Vikova, M., HRUBOSOVA, Z., 2014. Surface topography of textile braille labelling, Proceedings of the 7th International Textile, Clothing & Design Conference-Magic World of Textiles, Dubrovnik Available from: https://www. researchgate. net/publication/270957631_Surface_Topography_of_Textile_Braille_Labelling [accessed Aug 07, 2018].

Wang, H.-L., Chen, R.-P., Liu, Q.-W., Kang, X., 2019a. Investigation on geogrid reinforcement and pile efficacy in geosynthetic-reinforced pile-supported track-bed. Geotext. Geomembranes. 47, 755-766.

Wang, H.-L., Chen, R.-P., Liu, Q.-W., Kang, X., Wang, Y.-W., 2019b. Soil–geogrid interaction at various influencing factors by pullout tests with applications of FBG sensors. J. Mater. Civil Eng. 31, 04018342.

Wang, H.-L., Zhou, W.-H., Yin, Z.-Y., Jie, X.-X., 2019c. Effect of grain size distribution of sandy soil on shearing behaviors at soil–structure interface. J. Mater. Civil Eng. 31, 04019238.

Wang, J., Gutierrez, M.S., Dove, J.E., 2007. Numerical studies of shear banding in interface shear tests using a new strain calculation method. Int. J. Numer. Anal. Met. 31, 1349-1366.

Wang, J., Jiang, M., 2011. Unified soil behavior of interface shear test and direct shear test under the influence of lower moving boundaries. Granul. Matter 13, 631-641.

Wang, J., Liu, S., Cheng, Y.P., 2017. Role of normal boundary condition in interface shear test for the determination of skin friction along pile shaft. Can. Geotech. J. 54, 1245-1256.

Wang, X., Wang, X.-Z., Zhu, C.-Q., Meng, Q.-S., 2019d. Shear tests of interfaces between calcareous sand and steel.

Mar. Georesour. Geotec. 37, 1095-1104.
Wang, Z., Jacobs, F., Ziegler, M., Yang, G., 2020. Visualisation and quantification of geogrid reinforcing effects under strip footing loads using discrete element method. Geotext. Geomembranes. 48, 62-70.
Wu, X.-Y., Yang, J., 2016. Direct shear tests of the interface between filling soil and bedrock of Chongqing airport. Advances in civil, envrionmental, and materials research (ACEM16), Jeju Island.
Yavari, N., Tang, A.M., Pereira, J.-M., Hassen, G., 2016. Effect of temperature on the shear strength of soils and the soil–structure interface. Can. Geotech. J. 53, 1186-1194.
Yuen, K.-V., Ortiz, G.A., Huang, K., 2016. Novel nonparametric modeling of seismic attenuation and directivity relationship. Comput. Method Appl. M. 311, 537-555.
Yuen, K.V., Ortiz, G.A., 2016. Bayesian nonparametric general regression. Int. J. Uncertain Quan. 6.
Zhang, N., Evans, T.M., 2018. Three-dimensional discrete element method simulations of interface shear. Soils Found. 58, 941-956.
Zhao, L.-S., Zhou, W.-H., Fatahi, B., Li, X.-B., Yuen, K.-V., 2016. A dual beam model for geosynthetic-reinforced granular fill on an elastic foundation. Appl. Math. Model. 40, 9254-9268.
Zhao, L.-S., Zhou, W.-H., Su, L.-J., Garg, A., Yuen, K.-V., 2019. Selection of Physical and Chemical Properties of Natural Fibers for Predicting Soil Reinforcement. J. Mater. Civil Eng. 31, 04019212.
Zhou, G.-Q., Xia, H.-C., Zhao, G.-S., Jie, Z.J.J.o.C.U.o.M., Technology, 2007. Nonlinear elastic constitutive model of soil-structure interfaces under relatively high normal stress. J. China Uni. Mining Tech. 17, 301-305.
Zhou, W.-H., Jing, X.-Y., Yin, Z.-Y., Geng, X., 2019. Effects of particle sphericity and initial fabric on the shearing behavior of soil–rough structural interface. Acta Geotech. 1-18.
Zhou, W.-H., Yuen, K.-V., Tan, F., 2012. Estimation of maximum pullout shear stress of grouted soil nails using Bayesian probabilistic approach. Int. J. Geomech. 13, 659-664.
Zhu, H., Zhou, W.-H., Yin, Z.-Y., 2017. Deformation mechanism of strain localization in 2D numerical interface tests. Acta Geotech. 1-17.
Zhu, H.X., Zhou, W.H., Jing, X.Y., Yin, Z.Y., 2019. Observations on fabric evolution to a common micromechanical state at the soil‐structure interface. Int. J. Numer. Anal. Met. 43, 2449-2470.

Table

Table. 1 Review of recent studies on the effect of morphology parameters on soil-structure interactions

Authors	**Surface pattern**	**Quantified parameter**	**Selected results**
Chen et al. (2015)	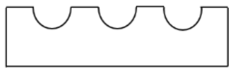	Average depth of the poured sand	● The shear strength increases with the surface roughness. ● The shear failure plane is dependent with the confining pressure and surface roughness.
Chu and Yin (2005)	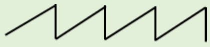	Roughness angle	● The surface roughness has great impact on the interface shear strength.
Dove and Jarrett (2002)		Asperity angle Root spacing Asperity spacing Asperity height	● The interface behavior is influenced by predictable geometric properties. ● The proposed mechanical equation can be applied to complex manufactured surfaces.
Feng et al. (2018)	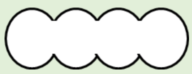	Relative roughness	● Stronger interaction between soil and geomembrane was developed under rougher geomembrane shearing.
Chen et al. (2020); Hu and Pu (2004); Jing et al. (2018); Su et al. (2018); Wang et al. (2019c); Zhu et al. (2017)		*Relative roughness*	● There exists a critical roughness to affect the interface shear strength
Zhang and Evans (2018)		*Relative roughness*	● For smoother interfaces, the contact normal force decays more rapidly

			compared to rougher interfaces.
Guo et al. (2020); Wang et al. (2019d)		*Flat width Intersection angle Groove depth*	● Peak shear stress increases with normal stress and the intersection angle
Canakci et al. (2016); Han et al. (2018); Martinez and Frost (2017); Rui et al. (2020)	*Random*	*Normalized average of maximum roughness, Average roughness*	● The larger interface friction angle was found for the case of rougher interface shearing.

Table 2. Components of the used concrete

Material	**Dosage**	**Material**	**Dosage**
Portland cement (Type II A-LL 42.5 R)	352 kg	Plasticizer Sika® viscoflow®-6920	2.0 L
Water	165 L	Crushed basalt aggregates	1086.6 kg
Fine aggregate	724.4 kg		

Table 3. Morphology parameters in accordance with standard ISO 4287 (ISO, 2009)

Morphology parameters	**Parameter**	**Definition**	**Description**
Amplitude parameters	Maximum profile peak height: Pp	The maximum height value	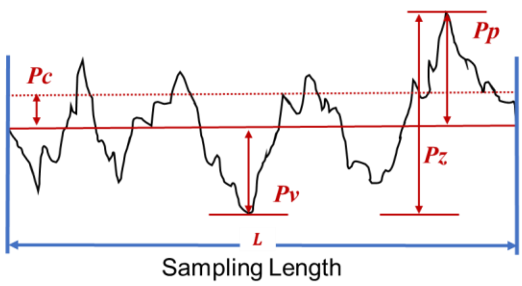
	Maximum profile valley depth: Pv	The minimum height value	
	Maximum height	The difference between the	

of the profile: Pz	maximum height and the minimum height	
Arithmetic mean deviation of the profile: Pa	$Pa = \frac{1}{n}\sum_{i=1}^{n}\lvert Z_i\rvert$ where n is the number of points and Z_i is the height value at point i.	
Mean height of profile elements: Pc	$Pa = \frac{1}{n}\sum_{i=1}^{n}\lvert Zt_i\rvert$	This represents the mean for the height Zt of profile elements within the investigated sampling length
Root mean square deviation of the profile: Pq	$Pq = \sqrt{\frac{1}{n}\sum_{i=1}^{n} Z_i^2}$	This is one of the most widely used parameters and is also referred to as the RMS value.
Skewness of the profile height distribution: Psk	$Psk = \frac{1}{Pq^3}(\frac{1}{n}\sum_{i=1}^{n} Z_i^3)$	If this parameter is zero, it means that the height distribution is symmetric. Positive Psk represents the surfaces possessing fairly high spikes or peaks that protrude above a flatter average. Reversely, Surfaces with fairly deep valleys and scratch in a smoother plateau such as porous surfaces, lead to negative Psk.
Kurtosis of the profile height distribution: Pku	$Pku = \frac{1}{Pq^4}(\frac{1}{n}\sum_{i=1}^{n} Z_i^4)$	The Pku describes the sharpness of the height distribution. Surfaces normally possess relatively few high peaks and low valleys when kurtosis is smaller than 3. In contrast, surfaces with many high peaks and low valleys lead to a kurtosis value of more than 3.

Spacing parameters	Mean width of profile elements: PSm	The mean width of profile elements are neighboring peak-valley pairs.	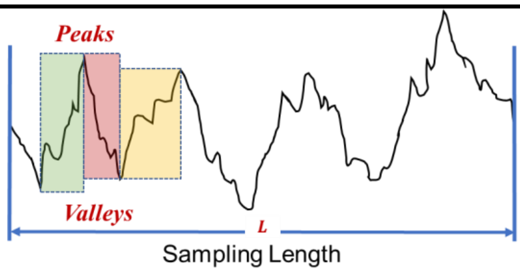
Hybrid parameters	Root mean square slope of the profile: Pdq	$Pdq = \sqrt{\frac{1}{n}\sum_{i=1}^{n}(\frac{dZ_i}{dx})^2}$	This represents the root mean square for the local slope within the sampling length.
Material ratio curves and related parameters	Material ratio of the profile: Pmr	The ratio between the material length and the evaluation length for the section height level C (% or µm).	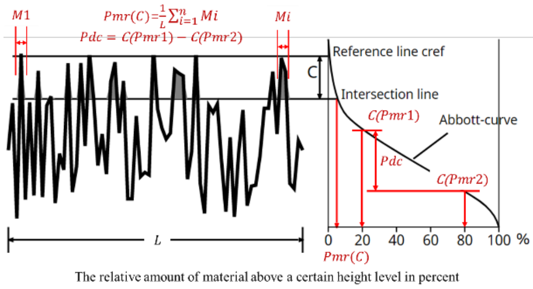
	Relative material ratio of the profile: Pdc	Signifies the height difference in section height level C, matching the two material ratios.	
Peak parameter	Number of peaks: PPc	Number of peaks per unit length	

Table 4. The selected input parameters (Zhu et al., 2017)

Parameters	**Value**
Ball density (kg/m^3)	2650
Inter-particle normal stiffness k_n (N/m)	5.0×10^9
Inter-particle shear stiffness k_t (N/m)	2.5×10^9
Particle-wall normal stiffness k_{nw} (N/m)	9.0×10^9
Particle-wall shear stiffness k_{tw} (N/m)	4.5×10^9
Inter-particle frictional coefficient f_p	0.5

Particle- boundaries frictional coefficient f_{pw}	0.9
Rolling resistance coefficient μ_r	0.1

Table 5. Experimental program for 480 simulated interface shear tests

Type of concrete profile	Number of profiles	Mean diameter D_{50}	Uniformity coefficient	Total groups
T1	60	D_{50} = 0.35 mm (30 groups) D_{50} = 0.53 mm (60 groups) D_{50} = 0.80 mm (30 groups)	1.46	120
T2	60	D_{50} = 0.35 mm (30 groups) D_{50} = 0.53 mm (60 groups) D_{50} = 0.80 mm (30 groups)	1.46	120
T3	60	D_{50} = 0.35 mm (30 groups) D_{50} = 0.53 mm (60 groups) D_{50} = 0.80 mm (30 groups)	1.46	120
T4	60	D_{50} = 0.35 mm (30 groups) D_{50} = 0.53 mm (60 groups) D_{50} = 0.80 mm (30 groups)	1.46	120

Table 6. Statistical characteristics of 13 morphology parameters and measured peak interface efficiency IE_P based on the results of 480 interface shear tests

Morphology parameter		**Mean**	**Standard deviation**	**Skewness**	**Kurtosis**	**Minimum value**	**Maximum value**
Amplitude parameters	Pp/D_{50}	1.5024	1.84427	3.288	12.763	0.23	13.80
	Pv/D_{50}	1.3171	1.59315	3.264	11.681	0.28	10.59
	Pz/D_{50}	2.8193	3.34616	3.135	10.777	0.62	21.08
	Pc/D_{50}	1.1783	1.46368	2.902	9.360	0.23	9.46
	Pa/D_{50}	0.4177	0.50005	3.143	11.451	0.09	3.63
	Pq/D_{50}	0.5269	0.62203	3.014	10.226	0.11	4.29
	Psk	0.1497	0.59633	0.288	2.081	-1.63	2.44
	Pku	3.3258	1.22181	2.705	9.626	2.12	10.29

Spacing parameters	PSm/D_{50}	3.4195	3.06364	3.667	17.643	0.76	28.12
Hybrid parameters	Pdq	36.3505	13.39251	1.186	2.455	9.68	75.98
Material ratio curves and related parameters	Pmr	0.2126	0.06687	0.521	3.312	0.10	0.49
	Pdc/D_{50}	0.8729	1.07105	3.277	12.591	0.18	7.97
Peak count parameter	PPc	6.1984	3.77133	0.464	-0.255	0.63	16.46
Predicted peak interface efficiency	IE_P	0.7051	0.08673	0.283	-0.240	0.52	0.94

Table 7. Calculated spearman's rank correlation coefficientfor 13 morphology parameters

Morphology parameters		SRCC
Amplitude parameters	Pp/D_{50}	0.554
	Pv/D_{50}	0.541
	Pz/D_{50}	0.562
	Pc/D_{50}	0.551
	Pa/D_{50}	0.546
	Pq/D_{50}	0.548
	Psk	0.102
	Pku	-0.055
Spacing parameters	Psm/D_{50}	-0.485
Hybrid parameters	Pdq	0.777
Material ratio curves and related parameters	Pmr	-0.029
	Pdc/D_{50}	0.543
Peak count number	PPc	0.459

Table 8. Results of some selected models based on the BNGR algorithm

Model	**Smoothing scale parameter** v_1	**Perdition error scale parameter** v_2	**Maximum likelihood**	**Evidence** $p(y\|X, C^{(k)})$	**Plausibility** $p(C^{(k)}\|y, X)$
(x_8)	0.0287	33.3831	2.91×10^{-189}	3.76×10^{-196}	0.999

$(x_8,\ x_{10})$	0.0337	17.9378	3.05×10^{-195}	4.63×10^{-202}	1.2×10^{-6}
$(x_5,\ x_8)$	0.0018	23.9538	4.07×10^{-194}	1.06×10^{-202}	2.8×10^{-7}
$(x_4,\ x_8)$	0.0039	26.4244	4.36×10^{-201}	3.16×10^{-209}	8.4×10^{-14}
$(x_8,\ x_9)$	0.0042	26.3362	2.30×10^{-201}	1.70×10^{-209}	4.5×10^{-14}
$(x_6,\ x_8)$	0.0033	26.5100	1.74×10^{-201}	1.16×10^{-209}	3.1×10^{-14}
$(x_3,\ x_8)$	0.0145	27.9494	2.04×10^{-203}	4.16×10^{-210}	1.1×10^{-14}

Table 9. Accuracys measurement for some selected models

Model	**MAE**	**MARE**
Optimal model (x_8)	0.0345	0.0487
$(x_8,\ x_{10})$	0.0420	0.0596
$(x_5,\ x_8)$	0.0410	0.0583
$(x_4,\ x_8)$	0.0417	0.0589
$(x_8,\ x_9)$	0.0417	0.0593
$(x_6,\ x_8)$	0.0407	0.0580
$(x_3,\ x_8)$	0.0428	0.0609
(x_3)	0.0588	0.0853
Full model	0.0367	0.0520

Table 10. Accuracy measurements for the proposed formula and existing formulas

Equation	**MAE**	**MARE**
The proposed formula	0.0442	0.0631
Formula referred by Subba et al. [62]	0.0594	0.0841
Formula referred by Zhou et al. [63]	0.0589	0.0834
Formula referred by Sharma et al. [61]	0.0760	0.107

Figures

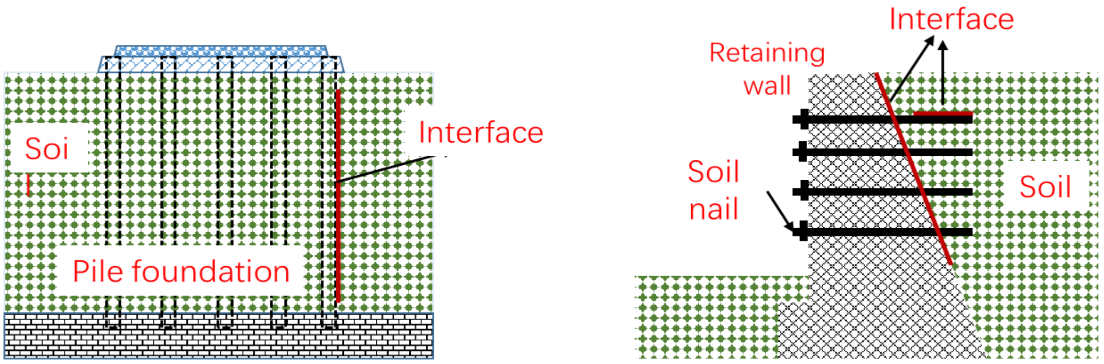

(a) Foundation engineering (b) Supporting engineering

Fig. 1. Common interface between soil and structure in geotechnical engineering

Definition of relative roughness: $R_n = \frac{R_{max}}{D_{50}}$

where R_{max} is the max height of structure; D_{50} is the mean particle size.

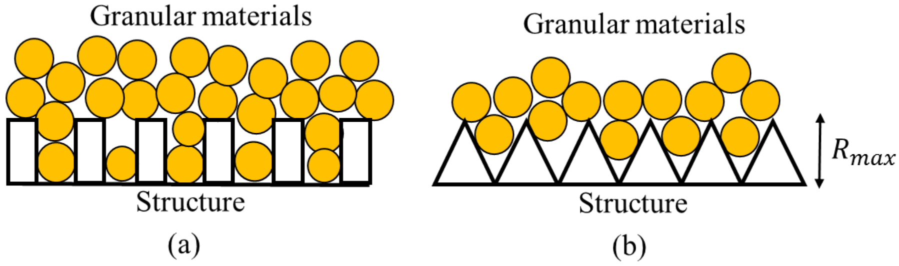

Fig. 2. Different rough profiles with the same relative roughness

Pp	Pv	Pz	Pc	Pa	Pq	Psk	Pku	PSm	Pdq	Pmr	Pdc	PPc
0.461	0.484	0.945	0.526	0.156	0.189	-0.412	2.616	6.435	18.000	0.100	0.338	1.554

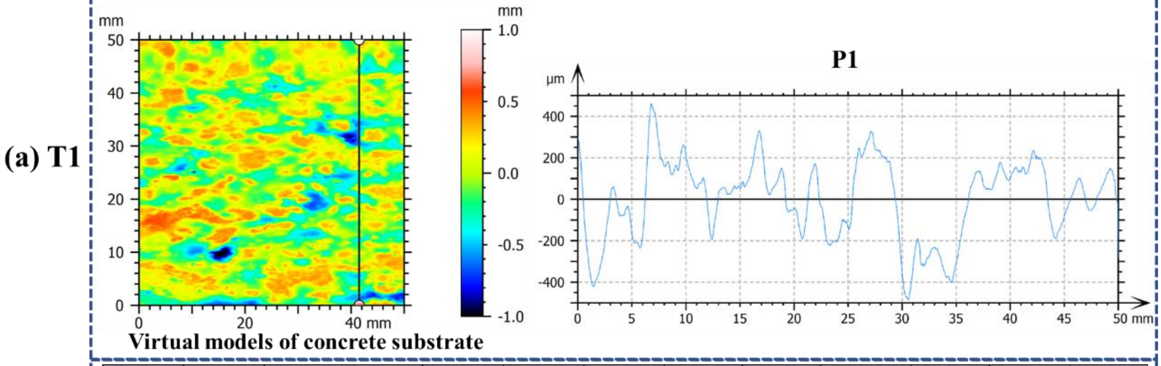

Pp	Pv	Pz	Pc	Pa	Pq	Psk	Pku	PSm	Pdq	Pmr	Pdc	PPc
0.372	0.222	0.594	0.215	0.091	0.115	0.748	3.289	1.840	28 .340	0.200	0.186	5.435

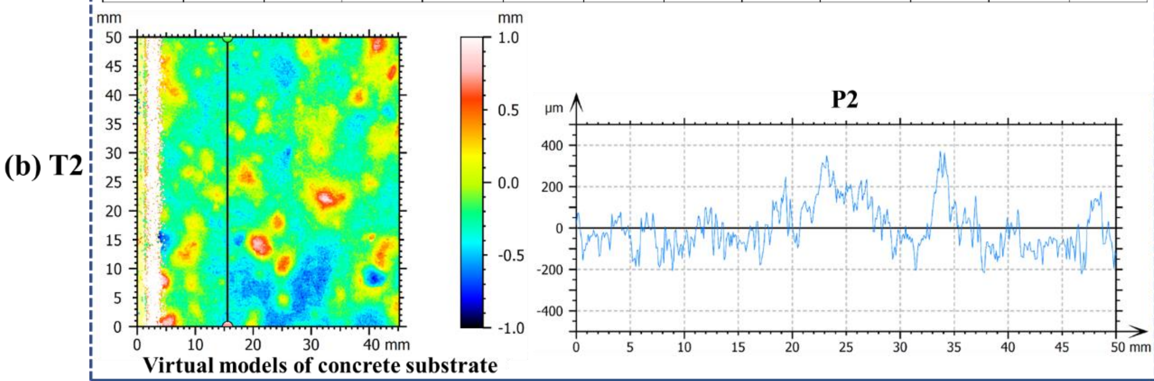

Pp	Pv	Pz	Pc	Pa	Pq	Psk	Pku	PSm	Pdq	Pmr	Pdc	PPc
0.380	0.354	0.734	0.306	0.098	0.126	0.168	3.109	1.383	36.420	0.246	0.205	7.228

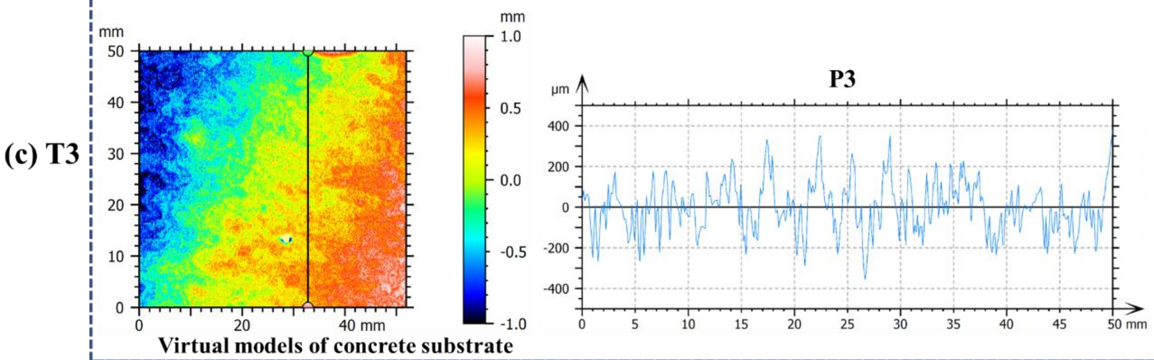

Pp	Pv	Pz	Pc	Pa	Pq	Psk	Pku	PSm	Pdq	Pmr	Pdc	PPc
0.371	0.319	0.690	0.267	0.084	0.112	0.012	3.787	1.052	39.150	0.246	0.165	9.505

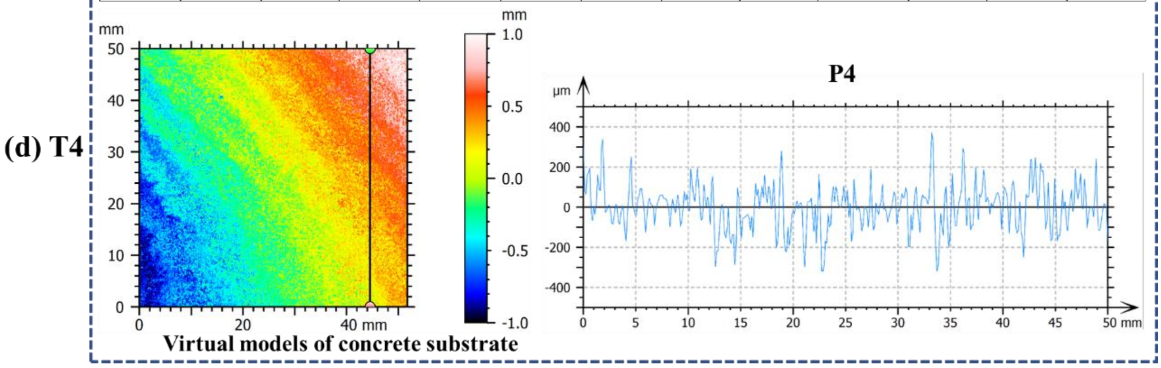

Fig. 3. 3D isometric views of four types of concrete substrates and their corresponding profiles

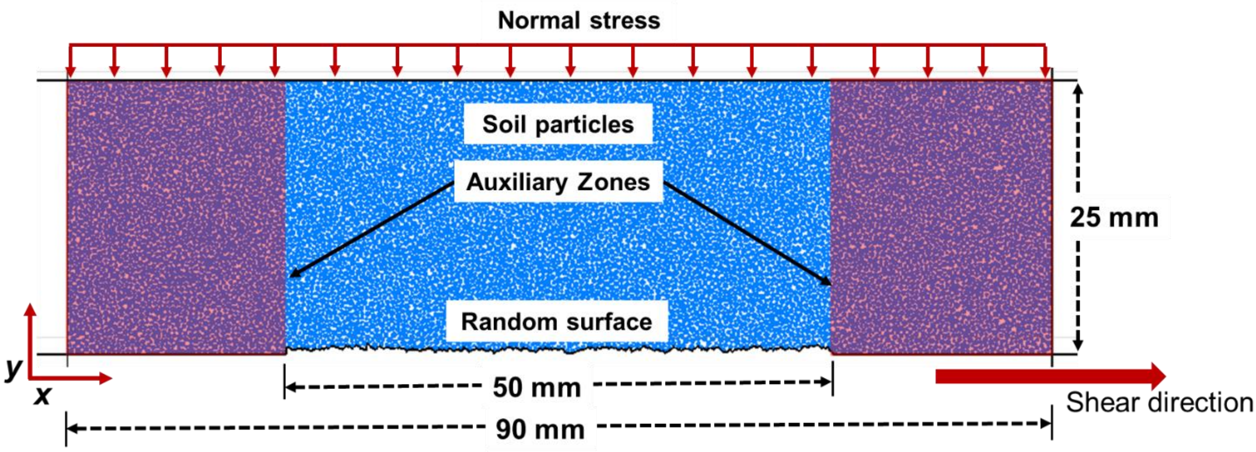

Fig. 4. Schematics of the interface shear apparatus with an imported random surface

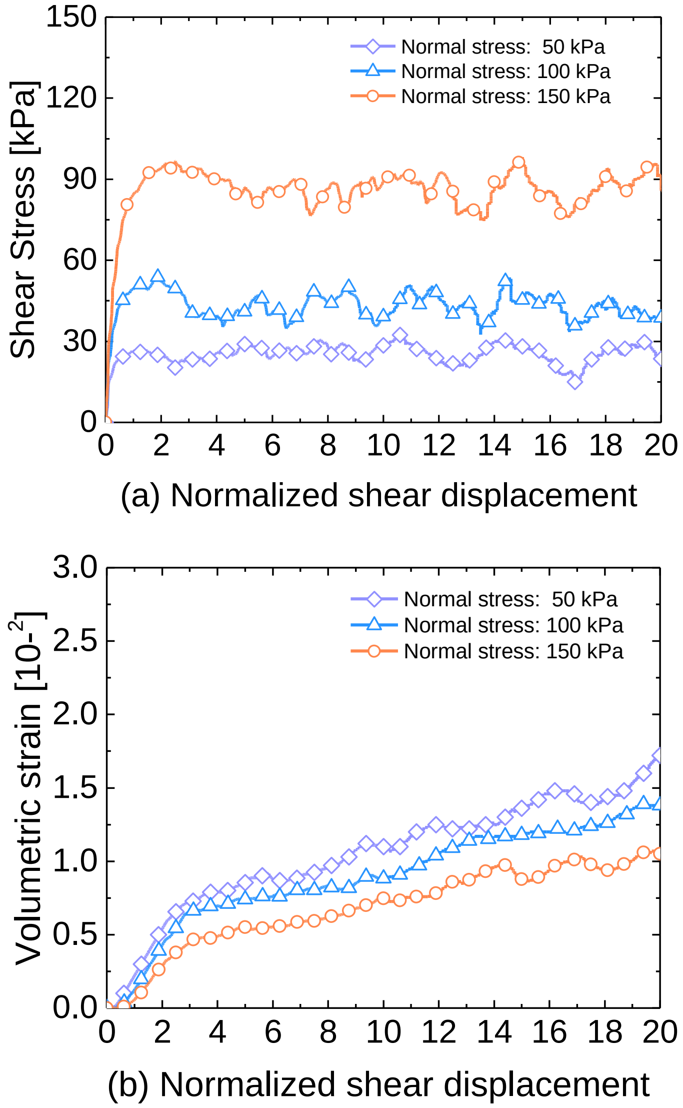

Fig. 5. Interface shearing behavior under various normal stresses: (a) shear stress versus normalized shear displacement and (b) volumetric strain versus normalized shear displacement

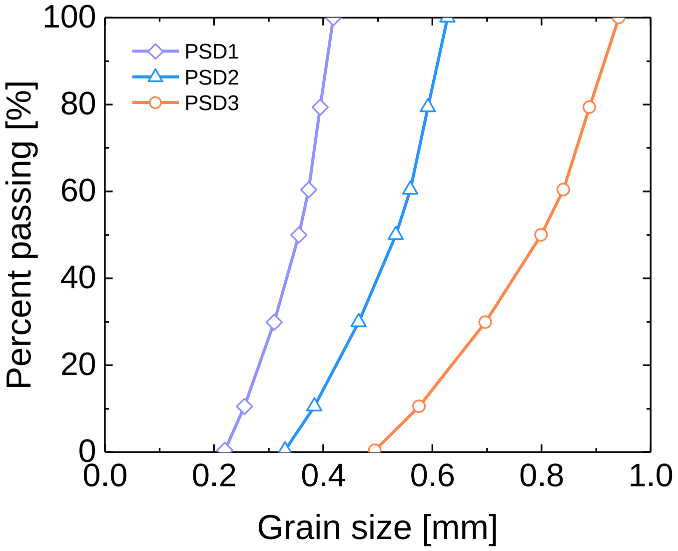

Fig. 6. The three particle size distributions with different mean particle sizes

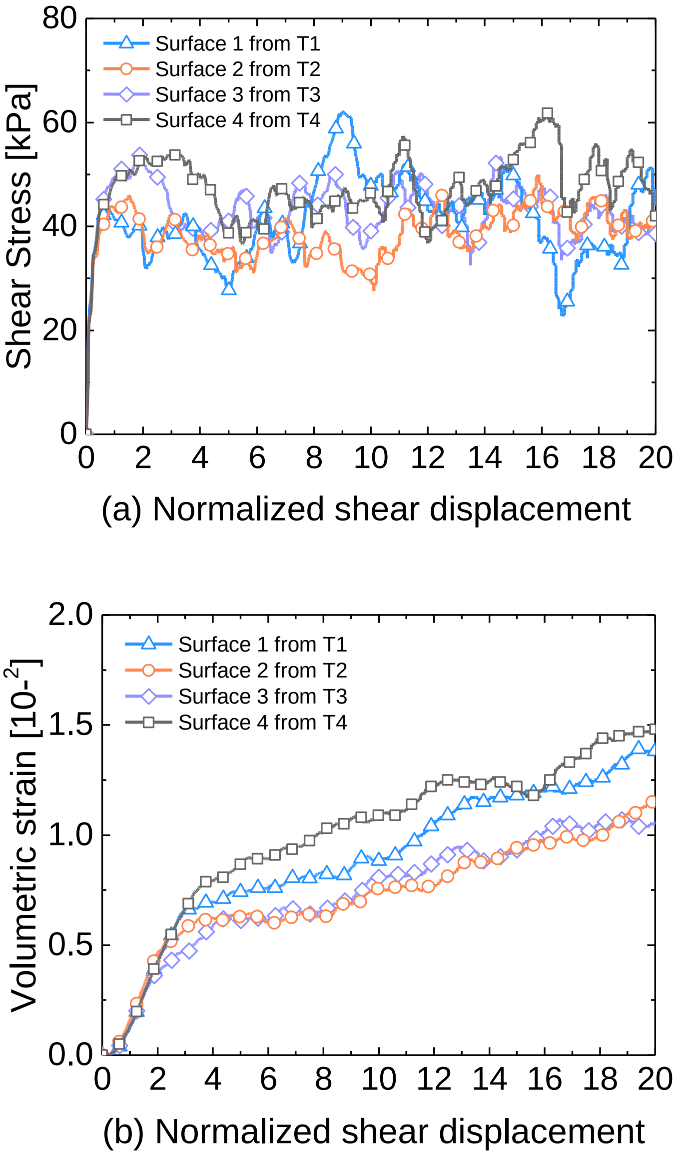

Fig. 7. Four typical macroscopic interface shearing behaviors: (a) interface efficiency versus normalized shear displacement and (b) volumetric strain versus normalized shear displacement

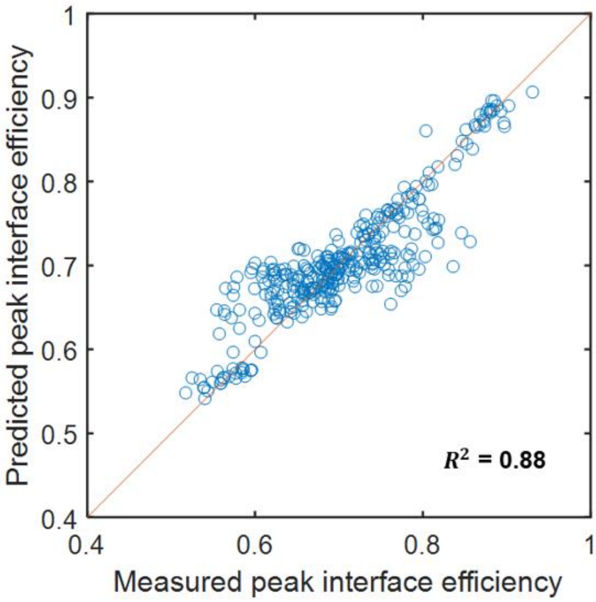

Fig. 8. Predicted peak interface efficiency based on the training dataset

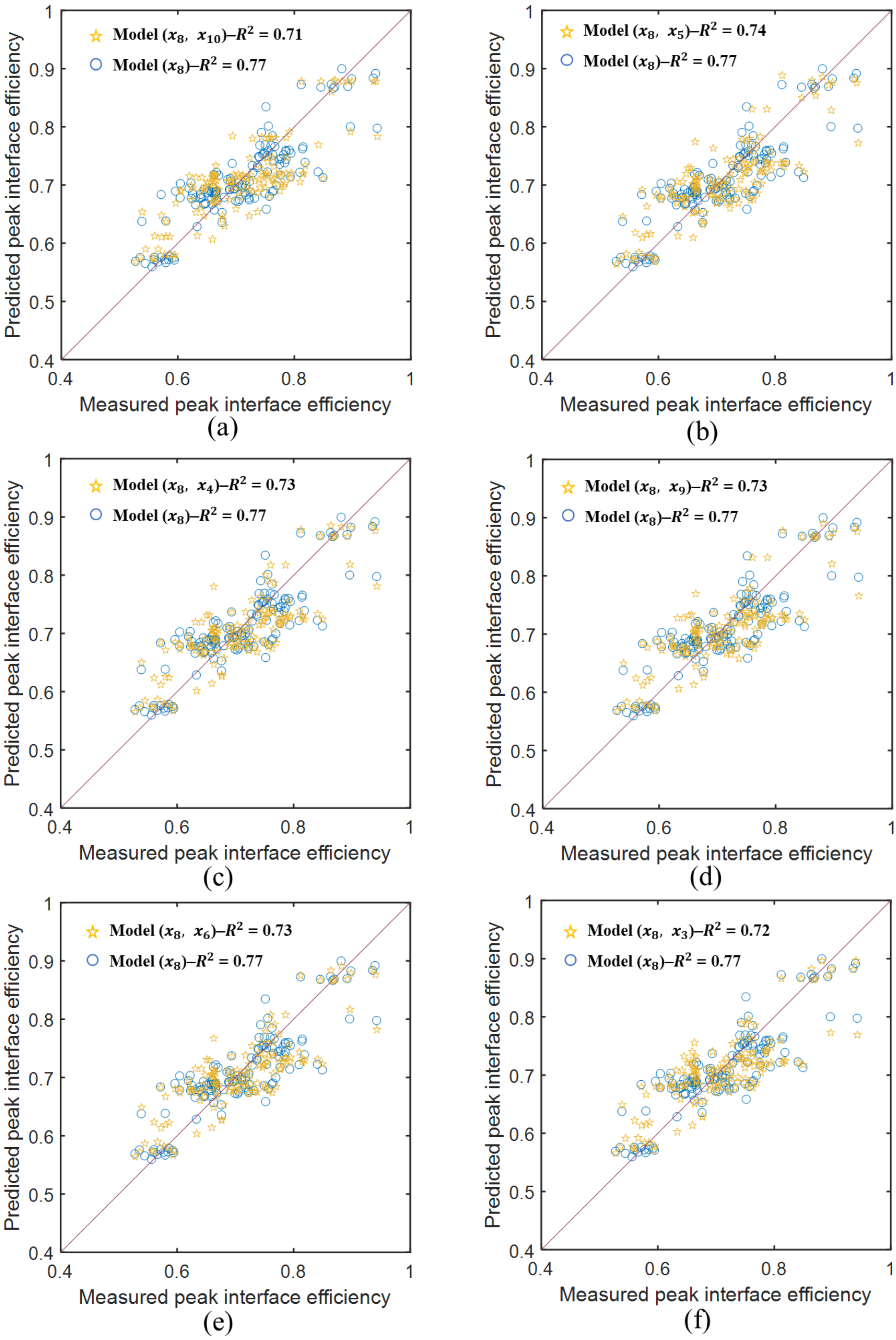

Fig. 9. Measured peak interface efficiency versus predicted peak interface efficiency using the optimal model and the models with two inputs

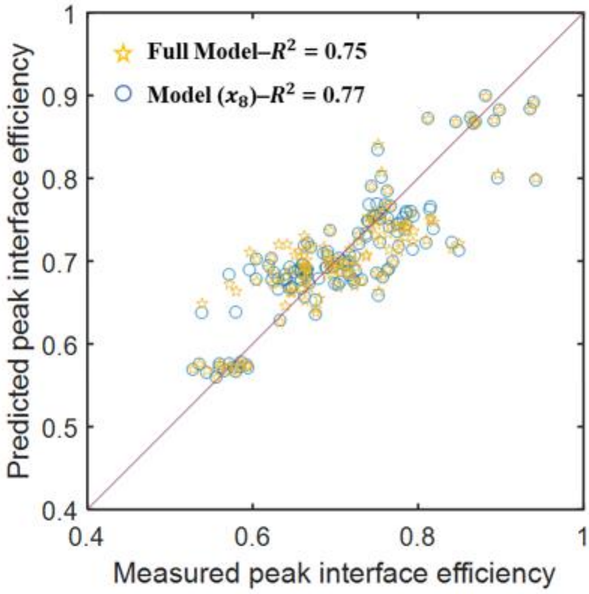

Fig. 10. Measured peak interface efficiency versus predicted peak interface efficiency using the optimal model and the full model

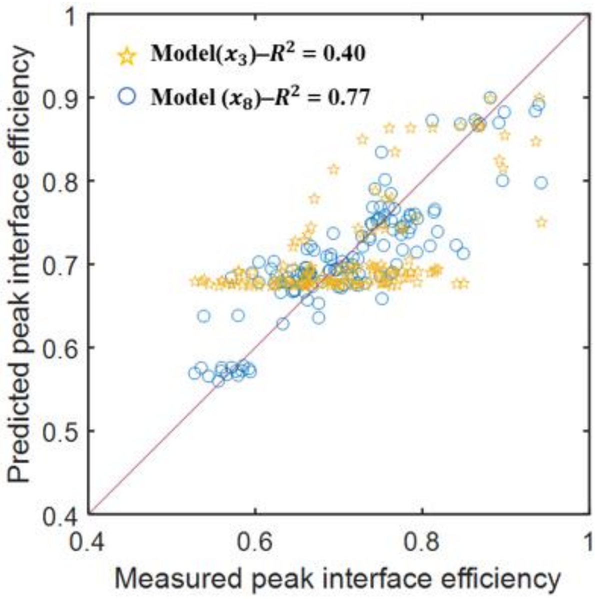

Fig. 11. Measured peak interface efficiency versus predicted peak interface efficiency using the optimal model and the models (x_3)

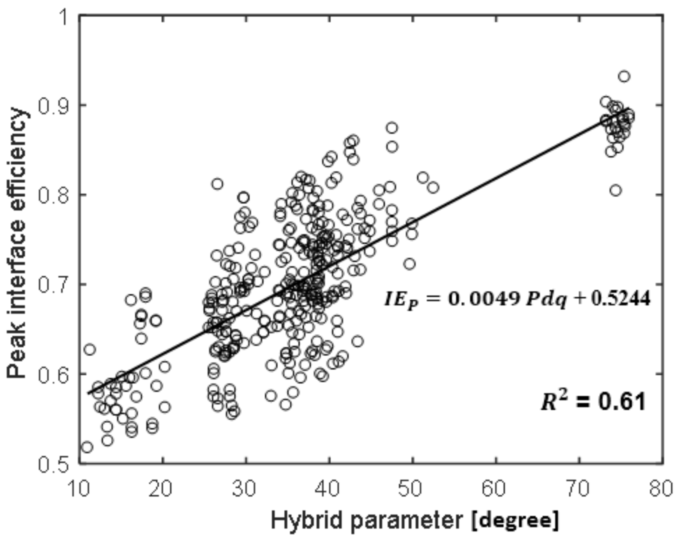

Fig. 12. Learning capability of the proposed formula and its expression

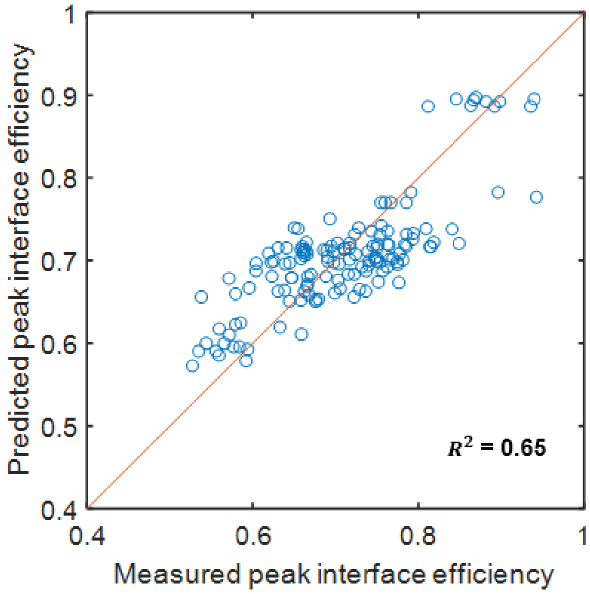

Fig. 13. Measured peak interface efficiency IE_P versus predicted peak interface efficiency IE_P using the proposed model

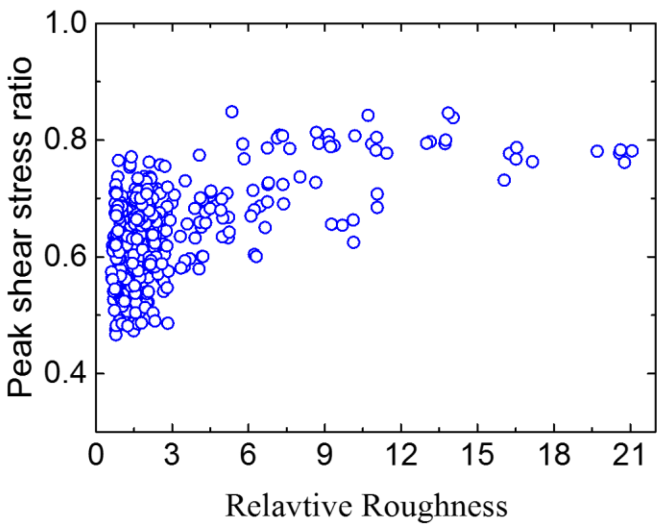

(a)

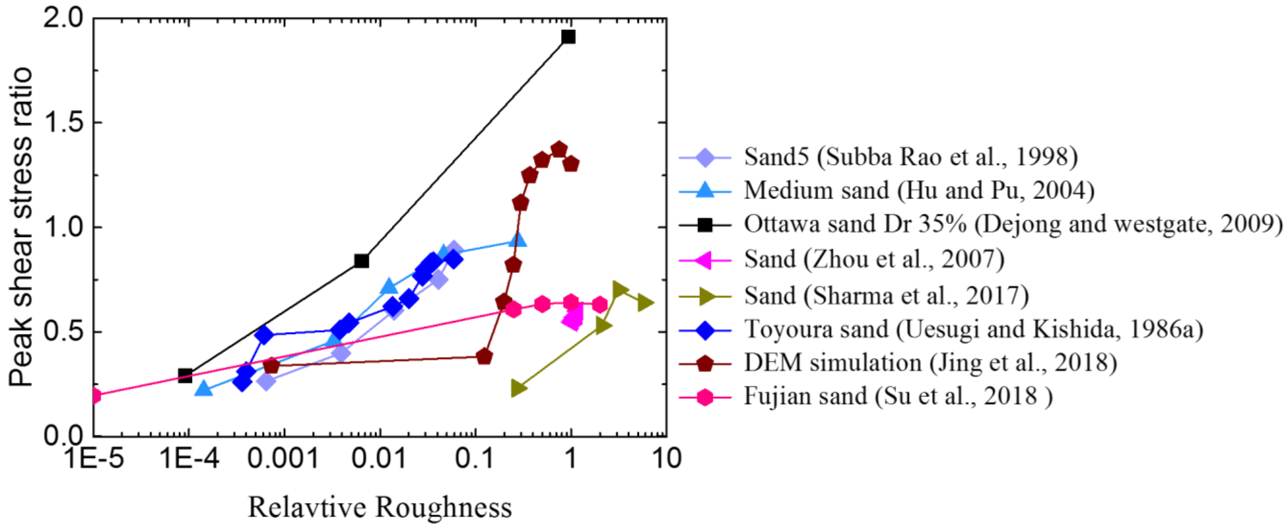

(b)

Fig. 14. Relationship between the peak interface strength parameter and relative roughness: (a) the present study and (b) other studies

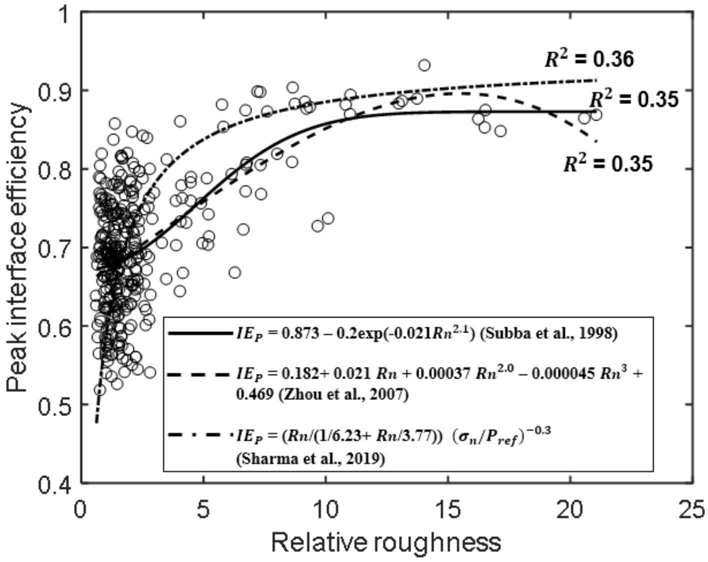

Fig. 15. Learning capability of the existing formulas and their expressions

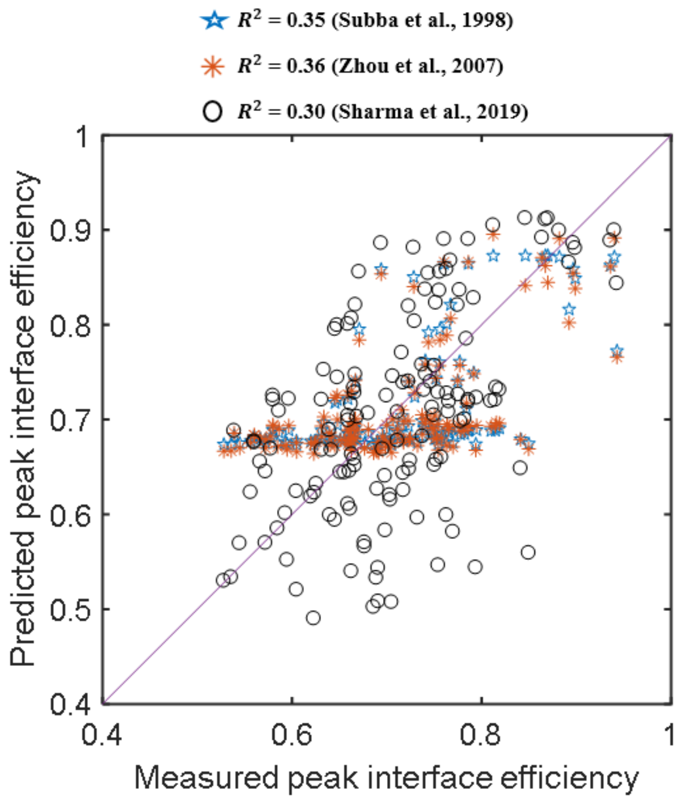

Fig. 16. Measured peak interface efficiency versus predicted peak interface efficiency using the existing formulas